MOBILE X-POL RADAR

A New Tool for Investigating Pyroconvection and Associated Wildfire Meteorology

Nicholas McCarthy, Hamish McGowan, Adrien Guyot, and Andrew Dowdy

The Bushfire Convective Plume Experiment examines the ability of portable, dual-polarized X-band radar to quantify the kinematics of pyroconvection through three case studies.

The broad range of scales at which wildfires interact with the atmosphere presents a complex problem for predicting the spread of wildfires and managing their impacts on natural and built environments. The importance of fire–atmosphere coupling has been acknowledged as early as the 1950s in wildfire reconstructions and "lessons learned" from postfire investigations (Byram and Nelson 1951; Graham 1951; Byram 1954; Robin 1957; Byram 1959). However, significant gaps remain in the quantitative analysis of the interaction of wildfires with the atmosphere on the scale of kilometers and less (Alexander and Thomas 2003; Potter 2012a,b). Addressing these knowledge gaps is an important research priority given that the risk of extreme fire behavior is thought to be increased by the influence of the pyroconvection on wind fields through changes in combustion rates and related rates of fire spread (Fromm et al. 2006; Cruz et al. 2012; Peterson et al. 2015). The lack of observational datasets on the storm scale (mesogamma) of fire events exhibiting extreme behavior represents a gap in our understanding of the pyroconvection process.

The process of pyroconvection occurs when fire-released heat, moisture, and/or aerosols induce or augment convection in the atmosphere. If this convection is sufficient for pyrocumulus cloud formation, then further development may subsequently lead to the formation of pyrocumulonimbus (pyroCb) (Fromm et al. 2010). Recent high-impact wildfires driven by intense pyroconvection include the Harvey–Waroona fire in Western Australia where 162 homes were lost (Ferguson 2016, 63–87) and the Fort McMurray fire in Alberta, Canada, which resulted in the evacuation of around 100,000 residents. Research of pyroCb has

AFFILIATIONS: McCarthy and McGowan—Atmospheric Observations Research Group, School of Earth and Environmental Sciences, University of Queensland, St. Lucia, Queensland, Australia; Guyot—School of Civil Engineering, University of Queensland, St. Lucia, Queensland, Australia; Dowdy—Research and Development Branch, Bureau of Meteorology, Melbourne, Victoria, Australia
CORRESPONDING AUTHOR: Nicholas McCarthy, nicholas.mccarthy@uq.edu.au

The abstract for this article can be found in this issue, following the table of contents.
DOI:10.1175/BAMS-D-16-0118.1

A supplement to this article is available online (10.1175/BAMS-D-16-0118.2)

In final form 22 November 2017

received significant attention in the past 10 years, especially in relation to its role in stratosphere injection of burned biomass, as well as some aspects of its feedback with fire dynamics (Fromm et al. 2006; Rosenfeld et al. 2007; Fromm et al. 2010; McRae et al. 2013, 2015; Peterson et al. 2015; Dowdy et al. 2017). Peterson et al. (2017b) offered a synoptic-scale conceptual model of pyroCb for western North America, highlighting key environmental elements for intense pyroCb development. In contrast, McRae et al. (2015) presented an analysis of the drivers of pyroconvection from the fire behavior perspective, examining fire progression and intensity, finding the terrain and fire intensity to be key precursors for pyroCb development.

The prediction of pyroconvection presents a set of complex problems for meteorologists and wildfire managers as operational forecast models do not currently take into consideration the influence of a fire on the atmosphere. This problem was highlighted during the Black Saturday wildfires in February 2009 in southeast Australia, where a number of distinct pyroconvective storms occurred, although forecast models did not indicate a high risk of thunderstorm development (Dowdy et al. 2017).

Plume dynamics represent a coupling mechanism between the synoptic weather driving pyroCb and forest fire dynamics. However, this is rarely examined within the context of pyroconvection (Morton 1957; Potter 2012b; Peace et al. 2015; Lareau and Clements 2016; Peterson et al. 2017a,b). Depending on the continuity of heat from the vegetation fire, convective updrafts will develop to form the plume that will bend into the ambient wind (Morton 1957). Associated updrafts will form into "puffs" as plume edge shear generates horizontal axis toroidal vortices (Morton 1957; Morton and Ibbetson 1996; Cunningham et al. 2005; Potter 2012b). Although such upward-pulsing structures in plumes have been well documented from a theoretical perspective, as well as in small grass fires, there has been limited investigation of larger forest fires where the winds are stronger and the heat release greater (McRae and Flannigan 1990; Morton and Ibbetson 1996; Clark et al. 1999; Clements et al. 2007). Coherent turbulent structures of the plume are also made up of vertical axis vortices, which may include counterrotating updrafts from plume bifurcation, or near-surface rotation in the form of fire whirls (Forthofer and Goodrick 2011). Both are known to occur in specific wind circumstances. However, the former is largely studied from an in-plume vorticity perspective, while simulations of the latter have focused on the fire characteristics such as geometry (Cunningham et al. 2005; Cunningham and Reeder 2009; Forthofer et al. 2009).

In forest fires (or bushfires in Australia), plume dynamics has significant implications for spotting—the process by which ignited fuels such as bark, leaves, and twigs known as firebrands are transported by the wind within and downwind of the plume, leading to further ignitions. The resulting spot fires can present major challenges to firefighters and can represent a potentially life-threatening hazard often far from the fire front (Koo et al. 2010). When convective plumes become vigorous, spotting distances become virtually impossible to predict deterministically. This has particular relevance in Australian conditions, where spotting has been reported to occur as far as 30 km downwind of wildfires (Cruz et al. 2012). Through large-eddy simulations, Thurston et al. (2017) demonstrated that previously studied turbulent structures play a significant role in the long-range transport of firebrands (Cunningham et al. 2005; Fric and Roshko 1994). Observations made by Lareau and Clements (2017) demonstrated the ability of scanning Doppler lidar to resolve the turbulent properties of a wildfire convective plume to validate the Briggs plume-rise equation, while in other field studies turbulence has been investigated at smaller scales (Seto et al. 2013, 2014; Heilman et al. 2015). However, there remain few quantitative observations of intense pyroconvective plume dynamics to validate the modeling of processes that drive long-range spotting, as reported by Cruz et al. (2012). While Clements and Oliphant (2014) demonstrate the capacity for rapid deployments of lidar to study wildfire plume dynamics, there is no work focusing on the possible role of deployable radar in this capacity.

Here, we present the rationale, strategy, and initial findings of the Bushfire Convective Plume Experiment (BCPE), a field-based study targeting quantitative observations of pyroconvection in southeast Australia. The BCPE aimed to address the problems of three-dimensional fire–atmosphere feedback processes at the scale of large (>1,000 ha) fire events where pyroconvection can occur. The findings highlight the utility of a mobile and quickly deployable, dual-polarized, X-band Doppler radar platform to resolve the coherent structures in turbulent plumes above wildfires. We present high-resolution radar observations of wildfires where the plume development is on the scale of kilometers vertically, resulting from rapid growth in fire area on an hourly time scale. These events were supplemented with data collection from large prescribed fires. The results are presented to highlight the utility of this approach and demonstrate its potential for use in future field campaigns studying pyroconvection. In particular, the benefit of dual-polarimetric Doppler

radar at a resolution capable of resolving the storm-scale structures of wildfire plumes is demonstrated, including within the context of enhancing the predictive capacity of fire behavior.

EXPERIMENTAL RATIONALE. The use of portable radar to investigate pyroconvection has gone almost entirely unexplored despite its extensive use during field campaigns studying thunderstorms and tornadogenesis in the United States (Bluestein et al. 1995; Wurman et al. 1997; Bluestein 1999; Biggerstaff et al. 2005; Wurman et al. 2012). The BCPE described here represents the first coordinated attempt to use mobile radar for analysis of large-scale fire–atmosphere dynamics. This comes at a time when compact radars with low power consumption are becoming more affordable, while simultaneously the costs of the effects of wildfires and their management challenges are rapidly increasing (McAneney et al. 2009; Haynes et al. 2010; U.S. Forest Service 2015).

While the use of radar in a supplementary capacity to study pyroconvection has been widely reported (Fromm et al. 2005; Rosenfeld et al. 2007; Fromm et al. 2010; Jones and Christopher 2010a; Potter 2012b; McRae et al. 2013, 2015; Lareau and Clements 2016), there is a paucity of data simultaneously collected to inform our understanding of the relationships between radar observations and fire behavior, and kinematics of the pyroconvection. Reid and Vines (1972) first delineate "turrets" from a forest fire, accounting for the horizontal and vertical plume evolution that provides more quantitative detail than do echo tops. Following reports by Rosenfeld et al. (2007) of the use of automated echo-top time series from operational radar, this approach has been used multiple times since to support remote sensing studies (Fromm et al. 2010; McRae et al. 2013, 2015; Dowdy et al. 2017). However, this method does not capture the turrets of individual updrafts as per Reid and Vines (1972). To date, the report by Banta et al. (1992) has been the only study where radar was used to identify kinematic structures within wildfire plumes, inferring plume bifurcation from Doppler velocity maxima. This is despite observations in multiple studies of the large-scale kinematic structures of wildfires, including the reported pyrogenic tornado in Canberra, Australian Capital Territory, Australia, in 2003 (Fromm et al. 2006; McRae et al. 2013). This is in contrast to the extensive use of mobile radars to observe thunderstorms, with the wide recognition of the ability of such methods to resolve structures and kinematics in convective plumes at much finer scales than operational radars (Bluestein et al. 2014).

The nature of the scatterers within the plume has been a notable impediment to the interpretation of radar observations of wildfire convection. Recent literature indicates that the radar beam scatterers within fire plumes are predominantly ash (Melnikov et al. 2008; Melnikov et al. 2009; Jones and Christopher 2010a,b; Lang et al. 2014; Lareau and Clements 2016). Baum et al. (2015) reported on the candidacy of large eucalypt ash (>2 mm^2) to be a Rayleigh-region scatterer at X-band frequencies using extensive statistical analysis. However, in situ studies of combustion by-products have only taken measurements away from the flaming region, such that the smoke, ash, and debris density, as well as the distribution closer to the fire, remain largely unknown (Radke et al. 1991). As noted by Reid et al. (2005), the equivalent mass and diameter of forest fire debris (including ash, carbon aggregates, partially burned foliage, and soil) can vary by up to a factor of 2 and be distributed over a complex range of geometries. In addition, Baum et al. (2015) highlight the importance of temperature and permittivity of ash particles acting as radar scatterers, largely unknown factors affecting their reflectivity properties. Given the importance of factors such as these that are currently not well understood, but which can fundamentally alter the scattering properties in radar observations, interpretation of wildfire signatures from radar observations needs to be based on a definition that acknowledges the uncertainties in the nature of the scatterers. Consequently, for the purposes of this paper we shall regard X-band scatterers in plumes under a purposefully broad definition of debris, including all airborne by-products of the fire greater than 2 mm^2.

The most recent investigations into fire with radar have highlighted the advantages of the polarimetric variables allowing better characterization of the debris and hydrometeors in convection above fires (Lang et al. 2014). Dual polarization can provide information on the differential reflectivity Z_{DR} and the correlation coefficient (CC) of the horizontally polarized and vertically polarized beams, where Z_{DR} is the difference between the two polarizations in the equivalent reflectivity factor, while CC expresses the correlation between the two polarizations in a value from zero to one. These metrics allow advanced interpretation of the radar scatterers, in the consistency of targets in CC (e.g., isotropic for rain droplets), and an indication of planarity and orientation with Z_{DR} (Chandrasekar et al. 2013). The results of Melnikov et al. (2009), Lang et al. (2014), and Lareau and Clements (2016) have consistently highlighted poor beam correlation (CC < 0.6) and strong differential reflectivity (Z_{DR} > 5) for the visible smoke regions

Table 1. Technical specifications of the UQ-XPOL radar.	
Manufacturer	Furuno, Nishinomiya, Japan
Model	WR-2100
Features	Dual-polarized (simultaneous) Doppler
Scan modes	Full-volume PPIs, sector RHI, sector PPIs, fixed-elevation PPI
Max power consumption	350 W
Peak power emitted	100 W
Beamwidth	2.7°
Antenna rotation speed	0.5–15 rpm
Z_H noise at 10 km	3 dBZ

of plumes, suggesting platelike targets consistent with debris. Above the condensation level, decreasing (increasing) Z_{DR} (CC) with height and also with proximity to the edges of the deep convective cloud was shown to be associated with lightning generation (Lang et al. 2014). To date, no study has examined the potential of dual polarization on portable radar platforms to study plume evolution or in-plume turbulence distribution pertinent to firebrand transport.

FIELD STRATEGY. At the core of the BCPE design is the first dedicated mobile dual-polarized Doppler X-band radar [the University of Queensland portable dual-polarized X-band Doppler radar (UQ-XPOL); Soderholm et al. 2016], which is combined with radiosondes, portable automatic weather stations (AWSs), and time-lapse cameras. This observational capability was adapted from the work of Soderholm et al. (2016), who investigated thunderstorm dynamics, with the UQ-XPOL radar detailed below (see Table 1). Figure 1 shows the radar during deployment to the Mount Bolton wildfire near Ballarat, Victoria (southeast Australia), with the accompanying equipment. (See animation Fig. ES4 in the online supplement for additional information: https://doi.org/10.1175/BAMS-D-16-0118.2.)

The BCPE adopts the well-established "storm chaser" experimental design of rapid and flexible deployment on a day-by-day basis, in collaboration with fire management operations. The fieldwork took place during two wildfire campaigns in the state of Victoria, and during two prescribed burning seasons in the state of Queensland, with one further wildfire campaign planned. The wildfire deployment strategy consists of a process of conditional checks, prioritizing the safety of crew and equipment while ensuring the observational objectives can be met. During the campaign, a threshold of the predicted forest fire danger index (FFDI; based on combining temperature, wind speed, relative humidity, and fuel moisture measures) greater than 50 triggers predeployments to regions

Fig. 1. The UQ-XPOL deployed during the Mount Bolton fire on 23 Feb 2016.

presenting the highest fire weather risk (McArthur 1967; Dowdy et al. 2009). It has been shown that, in Victoria, an ignition occurring when the FFDI is over 50 presents significantly decreased chances of "initial attack" suppression being successful in containing a fire (Hirsch and Martell 1996; Plucinski et al. 2012). Figure 2 synthesizes the joint operational and scientific requirements for field data collection during uncontrolled and potentially high-impact wildfires.

Based on the nature of most documented pyroconvection events, a fire area of 1,000 ha is used as the "rule of thumb" for the nominal minimum fire size in terms of predicted growth in a single day for major pyroconvection (McRae et al. 2015; Peterson et al. 2017a). Predictions are based on fire behavior analyst guidance, which is either provided remotely or, in some cases, by a support vehicle in the field. After an ignition capable of meeting this criterion is identified, the primary wind direction for the coming hours (and thus the initial spread axis of the fire) is determined to identify an exclusion zone. This allows for both safe observations and approach to the fire. Forecast wind changes are also assessed for their impacts on fire behavior and potential risks to the field team. Given the geographic constraints of safety, radar sensitivity, and possible ground clutter, wildfire deployments are largely confined to directly upwind locations.

The objectives of the field campaign are shaped around the priority to integrate with existing fire behavior products from which fire management decisions are typically made. These include aerial imagery (photography and multispectral line scanning) for fire-ground mapping, as well as postevent fire-ground assessment, including data collection of firebrands and spot-fire mapping (Cruz et al. 2014). The key dataset assembled from the synthesis of these products allows for the analysis of the fire intensity by area in mapping of the fire severity, and the fire's progression as isochrones of spread. By combining the available meteorological and fire analysis datasets, the BCPE analysis aims to bridge the two approaches to high-impact fire–atmosphere coupled events, with the goal of improving our nowcasting of wildfire behavior.

In addition to the opportunistic nature of the storm-chaser type of approach required for obtaining observations of wildfire events, data have also been collected in the field from several prescribed fires in collaboration with fire and land management agencies. Importantly, the prescribed burns allowed

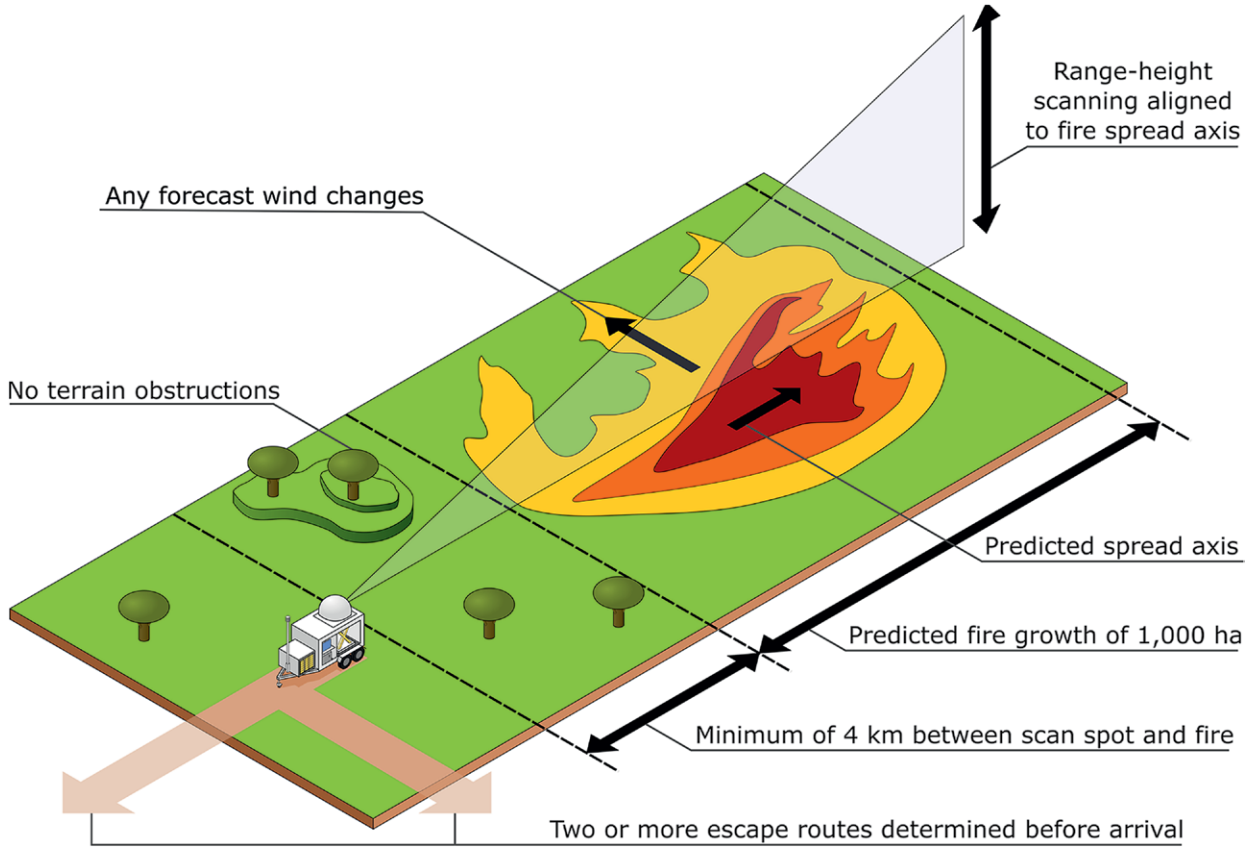

Fig. 2. The key requirements for wildfire deployments during the BCPE field campaign.

FIRE WEATHER OF THE PRESENTED CASE STUDIES

The synoptic conditions associated with the Mount Bolton fire event were typical of extreme fire weather conditions in southeast Australia, including an approaching cold front to the southwest, as well as a blocking high pressure system over the Tasman Sea to the east of Victoria. This set of conditions resulted in strong winds advecting hot and dry air from central inland regions over southeast Australia. A trough preceding this frontal system passed over the region during the afternoon of the fire event, resulting in a change from northwesterly to southwesterly winds.

The Dereel fire occurred under conditions that were somewhat similar to those of the Mount Bolton fire, with a blocking high to the east and an approaching cold front to the southwest. However, the front was farther away (to the southwest) in the case of the Dereel fire, with lower maximum temperatures on that day for the Dereel fire (i.e., 28°C, as compared to about 38°C for the Mount Bolton fire), based on a gridded analysis of station observations (Jones et al. 2009).

The Apsey West fire occurred under weaker synoptic conditions, with light westerly winds to the east of a ridge and a high pressure system in the Coral Sea, resulting in broad subsidence. Figures ES1–ES3 of the supplemental material show the synoptic analyses for all three events as shown by the Bureau of Meteorology's operational maps of mean sea level pressure fields and synoptic features.

for the preplanned deployment of both radar and AWS in a network to quantify the local-to-mesoscale weather conditions. The prescribed fire events were not associated with as intense fire behavior as wildfire because of the relatively subdued fire weather conditions, and thus no fire behavior data were collected.

OVERVIEW OF INITIAL RESULTS. When complete, the field campaign of the BCPE will have spanned 2.5 years, covering three wildfire seasons and two prescribed burning seasons. To date, this has consisted of 27 field days, resulting in the observation of three wildfires and two prescribed burns with the UQ-XPOL. Table 2 provides an overview of the observations to date, the field strategy employed, and details of the fires and fuel types.

Here, we present a selection of the results from the first three of these fires, each focusing on a different capability of the X-band radar. These include the initial findings of reflectivity structures from the Dereel wildfire; the Doppler characteristics of the Apsey West prescribed burn in Queensland; and the dual-polarization and spectral-width results from the Mount Bolton wildfire. The Mount Bolton case also highlights the substantial room for further research into synthesizing radar and fire behavior datasets.

Reflectivity observations from the Dereel fire. In January and February of 2016, the UQ-XPOL was deployed to western Victoria through the peak of summer when drought conditions prevailed (Bureau of Meteorology 2016). The first wildfire observed by the UQ-XPOL was the Dereel fire, ignited at approximately 37.83°S, 143.81°E, on the afternoon of 13 February. The research team was deployed to a location 4 km upwind of the fire, which burned under prevailing northwesterly winds. The fire weather conditions for this case were relatively high for this particular location, with an FFDI value of 28 on the day, corresponding to a percentile of 98.4 (based on daily values at this location during the period 1950–2016). These FFDI values, as well as others noted throughout this study, are obtained from a fire weather database (Dowdy 2018) used operationally by the Climate Information Services of the Bureau of Meteorology. No primary fire behavior data were collected from the relatively small fire, but the event provided the proof of concept that UQ-XPOL was capable of observing plume dynamics. Figure 3 illustrates the plume dynamics captured in reflectivity Z_H as vertical cross sections in range–height indicator (or RHI) scans. The radar analysis here and elsewhere was completed using the open-source PyArt package (Helmus and Collis 2016).

No pyrocumulus development was observed during this fire, and the maximum height of returns was around 3 km AGL, with a peak Z_H of 30 dBZ within the plume. The results illustrate turret structures evolving rapidly over the 11-min sampling period shown (lines A–D in Fig. 3). A significant "puff" structure (line A) of the plume was observed to rise over a kilometer vertically in less than 11 min, transporting an increased amount of scattering debris from the fire, potentially including firebrands. The length of each sampling gate was approximately 50 m in length for the UQ-XPOL and the beams had effective radii of 230, 470, and 710 m at 5, 10, and 15 km, respectively, which was also true of the other events reported.

As the simplest observation of plume structure in the Z_H data above, the turrets of reflectivity in the Dereel event (lines A–D in Fig. 3) bear close similarity to those that have been well studied in large-eddy modeling within the context of wildfires (Cunningham et al.

Table 2. Details of each BCPE deployment to date, including the nature of the data collected, daily max FFDI, and associated return interval, fire, and fuel details.

Fire name	Date	Lat and lon (°)	Radar scan strategy	Supporting instrumentation and data	FFDI (percentile value)	Fire details	Fuel details
Dereel: Tibbets Road*	13 Feb 2016	−37.82, 143.81	RHI	Single AWS; little fire behavior data	28 (98.4)	121-ha wildfire in western Victoria; ignition by machinery	Heathy dry forest fuels; avg canopy height of 20 m; dominant species include red stringybark, red ironbark, and red box (all *Eucalypt* genus)
Mount Bolton: Laverys Road*	23 Feb 2016	−37.37, 143.68	RHI	Substantial fire severity and fire progression data collected; no mesonet data	55 (99.9)	1,222-ha wildfire in western Victoria resulting in the loss of three houses, 10 sheds, and 400 poultry; unknown ignition source	Hills herb-rich woodland fuels; avg canopy height of 25 m; dominant tree species include messmate stringybark, narrow-leaf peppermint, and manna gum (all *Eucalypt* genus); small blocks of pine plantations and a large immature blue gum plantation were also present
Cedar Creek	20 May 2016	−27.89, 153.19	Sector PPI	Mesonet of seven Hobo AWSs deployed; no fire severity data	21 (88.6)	Prescribed fire in southeast Queensland using hand and aerial ignition	Dominant tree species include brush box, ironbarks, bloodwoods, and forest red gums (all *Eucalypt* genus)
Apsey West*	18 May 2016	−28.25, 151.01	Full-volume PPI	Mesonet of seven Hobo AWSs deployed; no fire severity data	23 (97.8)	3,200-ha prescribed fire in southwestern Queensland using aerial ignition	Brigalow woodland fuels; avg canopy height of 12 m; dominant tree species include brigalow (*Acacia* genus) and belah (*Casuarina* genus)
Sedgerly Road	5–6 Dec 2016	−28.19, 151.04	Full-volume PPI	Substantial fire severity and fire progression data collected; no mesonet data	36 (98.4)	6,100-ha wildfire in southwestern Queensland; lightning ignition on 4 Dec 2016	Brigalow woodland; avg canopy height of 12 m; dominant tree species include brigalow (*Acacia* genus), belah (*Casuarina* genus), and cyprus pine

* This fire event is discussed in the text.

2005; Fric and Roshko 1994) but never documented at this resolution by radar. They offer insights into what was likely observed by Reid and Vines (1972) but in much finer detail. The discrete nature of the turrets examined here presents promise for tracking at high temporal resolution as the lines A–D in Fig. 3 do in a rudimentary capacity. The turrets examined are worthy of further research in the specific relationship of these structures of debris to the temperature perturbations and updrafts they highlight.

Doppler wind observations from the Apsey West prescribed burn. In contrast to the Dereel fire, the Apsey West prescribed burn occurred under less severe fire weather conditions (FFDI = 21, which corresponds to a percentile value of 88.6 for the area). The purpose of this large burn in western Queensland (28.27°S, 151.02°E) was to reduce fuel loads in the 3,200-ha block by use of aerial ignitions in a 150-m grid pattern. The fire convergence from these ignitions led to the development of a convective plume that was stronger than would be expected for a single-point ignition given the conditions—a phenomenon known well in grid ignitions (McRae et al. 1989). The plan position indicator (PPI) observations of this plume by the UQ-XPOL indicated the presence of at least two vertical-axis vortex signatures within the plume. Figure 4 shows the evolution of these Doppler velocity (V_R) couplets at three

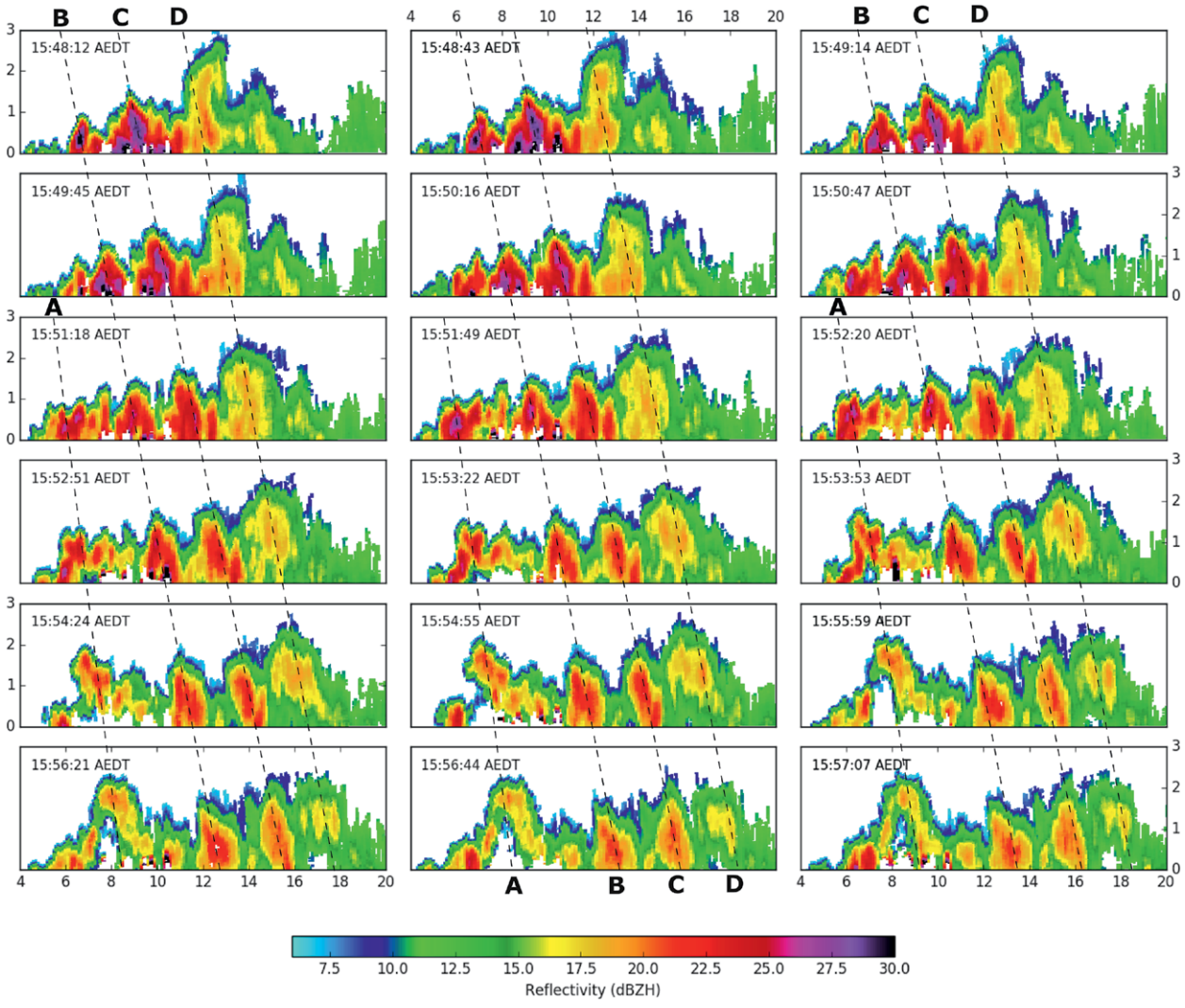

Fig. 3. A sequence of RHI scans showing the plume evolution of the 13 Feb 2016 Dereel fire at an average interval of 30 s between scans (progressing left to right). All scans are shown from a single-scan azimuth. Lines A–D intersect four turret features of the plume, illustrating their relative evolutions over time.

heights above the plume over 1 h, 20 min of the fire's lifetime (see also supplemental animation Fig. ES5).

Each of the two couplets in Fig. 4 appear to form in largely distinct plumes, with the bulk of the debris from the plume dissipating eastward (toward the right in Fig. 4), likely by detrainment as the plume expands, and fall out of debris at its base. The southern vortex feature (couplet A in Fig. 4) was most prominent, and reached its highest intensity at 1400 Australian eastern standard time (AEST = UTC + 10 h), 2 h after ignitions began at 1200 AEST. We adapt from Marquis et al. (2008) the concepts of using maximum tangential velocity (Max V_R) to calculate the maximum azimuthal wind shear (ΔV_R) as the difference between the peak inbound and outbound V_R. At 1400 AEST, couplet A had a maximum azimuthal wind shear of $\Delta V_R \approx 14$ m s^{-1} at a tilt of 6°. The vortex meandered very little over the full period shown in Fig. 4, and the consistent location of the signature across the three radar tilts indicated that the plume (in Z_H) and the associated vortex bent very little with height from the surface scans (350 m) to the observed top (1,200 m). Each of the scans after

▸ Fig. 4. PPI scans over the 18 May 2016 Apsey West prescribed burn from the UQ-XPOL at (left) 4°, (center) 6°, and (right) 8°. Each row is a scan volume beginning the nearest minute to 1320, 1340, 1400, 1420, and 1440 AEST. The Z_H contours are given every 5 dBZ. The UQ-XPOL is located 1 km outside of the plotted area, where the dashed reference lines converge in the bottom right. The pink boundary within each scan represents the perimeter of the prescribed burn, around which six mesonet weather stations are located. Wind barbs on each station are 5-min rolling averages (km h^{-1}) around the time of the scan.

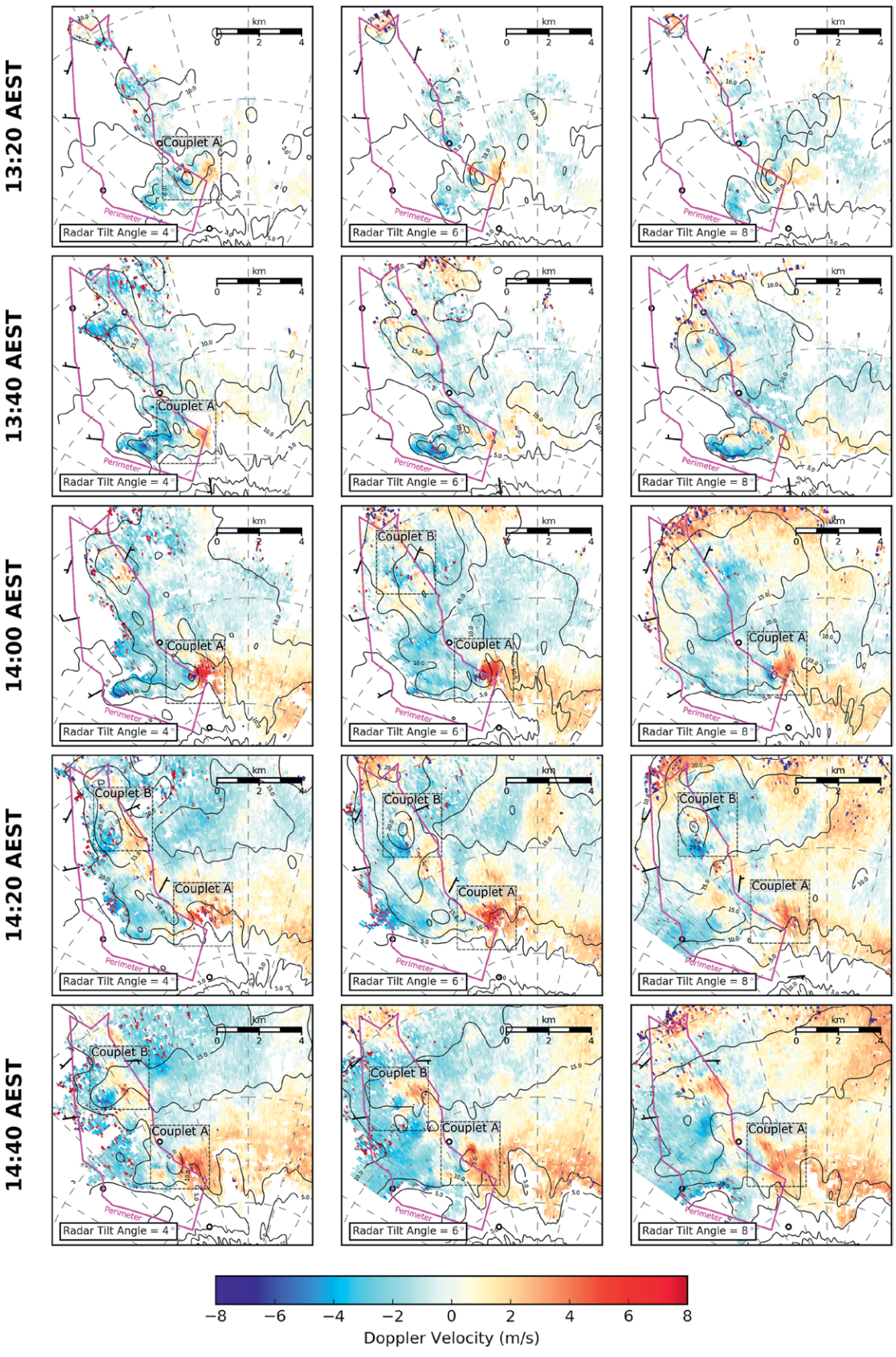

FIRE BEHAVIOR OF THE MOUNT BOLTON FIRE

Country Fire Authority ground observer teams documented the approximate locations of the Mount Bolton fire at 1415 and 1530 AEDT. Fire behavior analysts combined these locations, air observations at 1430 AEDT, and multispectral line scans at 1630 and 1830 to provide the fire estimates given in Fig. SB1 (see supplemental animations Figs. ES7 and ES8).

The fire reached approximately 126 ha within 30 min of first report at 1345 AEDT. Initially, the fire was fast burning through mixed stubble, grass, and patches of eucalypt woodland fuels (inside the 1415 AEDT perimeter in Fig. SB1a) with intermittent pyrocumulus formation (see Fig. ES6). The wind then changed from northwesterly to west-northwesterly, pushing the fire through more continuous eucalypt woodland fuels (dominantly messmate stringbark) mixed with small (<10 ha) pine forest blocks and through to the 1433 AEDT perimeter (Fig. SB1a). The large amount of short-range (<1 km) spotting off a ridge (Fig. SB1b; see Fig. ES7) led to a fast rate of spread of 7 ha min^{-1}, with additional long-range spotting occurring at a range of more than 1 km (Fig. SB1f).

In fire behavior, there is a well-known step change in intensity of fire when the fire fully engages with the canopy of the forest; this is known as a crown fire or "crowning" (Alexander and Cruz 2006). From 1433 to 1530 AEDT, the rate of spread was a slower 4 ha min^{-1}. In this zone, however, the fire burned through the crown of 32 ha of the forest, resulting in the largest continuous area of crowning and thus the highest severity during the fire (green stippling in Figs. SB1a,d). Figure SB1c shows an image of the significant coalescing spot fires at the southern end of the fire front; note that the front was approximately 3.6 km in length following the westerly wind change. The fire then increased in speed to 5 ha min^{-1} between 1530 and 1630 AEDT, again with significant spotting reported off the elevated terrain (Fig. SB1e; see Fig. ES8). By 1630 AEDT, the most active fire was burning through an immature blue gum plantation, contributing to rapid surface-driven spread though insignificant column development.

In total, eight spot fires were mapped in postfire field investigations outside the final burned area shown in Fig. SB1g, with the most significant at a distance of 6 km from the fire front. This was documented by helicopter shortly after its ignition at 1559 AEDT (Fig. SB1h).

► Fig. SB1. An overview of the Mount Bolton fire area and evidence of fire behavior. (a) Fire isochrones overlaid on postfire airborne multispectral (near IR, green–blue) vegetation imagery. Ground-validated areas of crown fire are shown in the green stippling. Locations of the photographs in the other panels are also marked. Height contours are given at 10-m spacing in white. (b) Aerial photograph of the plume during the early run of the fire. Spot fires can be seen beneath the plume being drawn in at a right angle to the prevailing wind. (c) Multiple spot fires are visible igniting and converging as the fire passes over a ridge. (d) A photograph of the full canopy combustion in a large area of crown fire from field mapping. (e) Aerial photograph of the plume after the fire intensity has peaked. A spot fire ignites in a blue gum plantation beneath the plume. (f) A spot fire ignites during the early run of the fire at approximately 1 km from the active fire front. (g) The UQ-XPOL location shown relative to the final burned area and several of the long-range spot fires that occurred beyond the final area [including the photos in this panel and (h)]. The scan azimuth of the UQ-XPOL RHI data presented (105°) is shown (blue dashed line), and the background shows prefire satellite imagery in the same spectral bands as (a). (h) A photograph of a spot-fire burn approximately 200 m in length at a distance of 6 km from the active fire front.

1340 AEST indicated a marked decrease in Z_H on the outbound (red) side of the couplet. This indicates that the debris of the plume was relatively confined within the boundary of the vortex, as was apparent in the sharp visible boundary of the plume (see Fig. ES5).

The second vertical vortex signature (couplet B in Fig. 4) was most intense at 1420 and 1440 AEST in the 6° and 8° tilts. It did not appear to share the same Z_H boundary features as couplet A and was, instead, associated with a circular, high-reflectivity (>25 dBZ) core from the plume. The maximum azimuthal shear at this stage was $\Delta V_R \approx 5$ m s^{-1} at 6°. Weaker rotational features were evident during other scans for both couplets A and B (e.g., 1320 AEST at 6° and 1440 AEST at 8° for A and B, respectively). Although most evident in couplet A, both features had their fastest rotation near the surface, decreasing with height.

Supporting the UQ-XPOL data from this event was a mesonet of seven weather stations deployed around the perimeter and at the radar-scan location. The wind barbs from the time of the vortex formation in the plume are shown in Fig. 4, indicating a large area of convergence at 1400 and 1420 AEST in the light winds. This was the only period during the fire in which notable convergence formed.

Whole-plume rotation has commonly been reported at fires in circumstances of light wind (e.g., McRae and Flannigan 1990) and was observed by Banta et al. (1992) by use of lidar. The weak synoptic conditions of the Apsey West prescribed burn enabled observations of the rotation in the plumes and the convergence evident in the mesonet. Only a small number of examples exist of vertical vortices in observations (Forthofer and Goodrick 2011), and they have never been noted

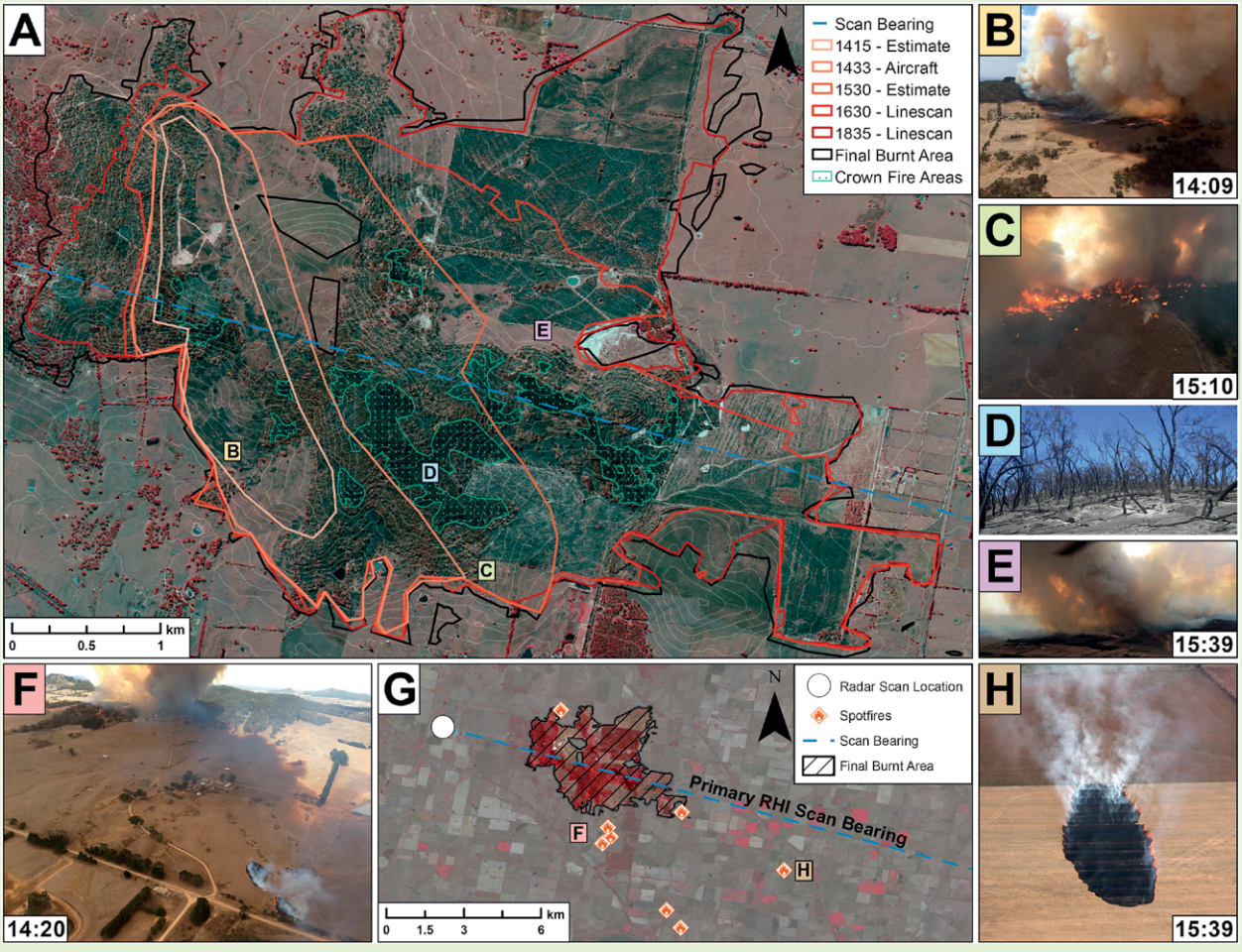

before in volumetric radar imagery. There are also some similarities with the boundary of the burn plot (a break in the fuel by access tracks) and the geometry of the fuels used to force convergence of the study fire whirls numerically (Forthofer et al. 2009). It is unclear if these vertical vortex features are a consequence of the combustion-generated vorticity, as in the case of a fire whirl, although no fire whirls were reported from the fire ground. Given the uncertainty of the origins of vorticity on this scale, there is an imperative to extend the observations of rotational signatures within plumes given they can significantly affect entrainment rates (Forthofer and Goodrick 2011). In addition, similar observations in larger fires could shed significant light on the debate around the nonsupercell genesis of pyrogenic tornadoes, such as was reported in the 2003 Canberra wildfire event (McRae et al. 2013).

Dual-polarization observations from the Mount Bolton wildfire. On 23 February 2016, the UQ-XPOL captured the development of the convective plume above the Mount Bolton fire, which evolved into a deep pyrocumulus. The team deployed to the Mount Bolton fire when reported at 1345 Australian eastern daylight savings time (AEDT = UTC + 11 h), with an estimated ignition point at 37.36°S, 143.68°E. The plume of the Mount Bolton fire was most intense through the period between 1520 and 1600 AEDT, as is shown in Fig. 5 (see also supplemental animation Fig. ES6).

The visual evolution of the plume is evident in Fig. 5 through the optical thickness, the bend in the plume, and the cloud development. From 1527 AEDT, a pyrocumulus cloud formed on top of the smoke column below the height of the visible stratiform cloud layer. From 1525 to 1440 AEDT, the plume

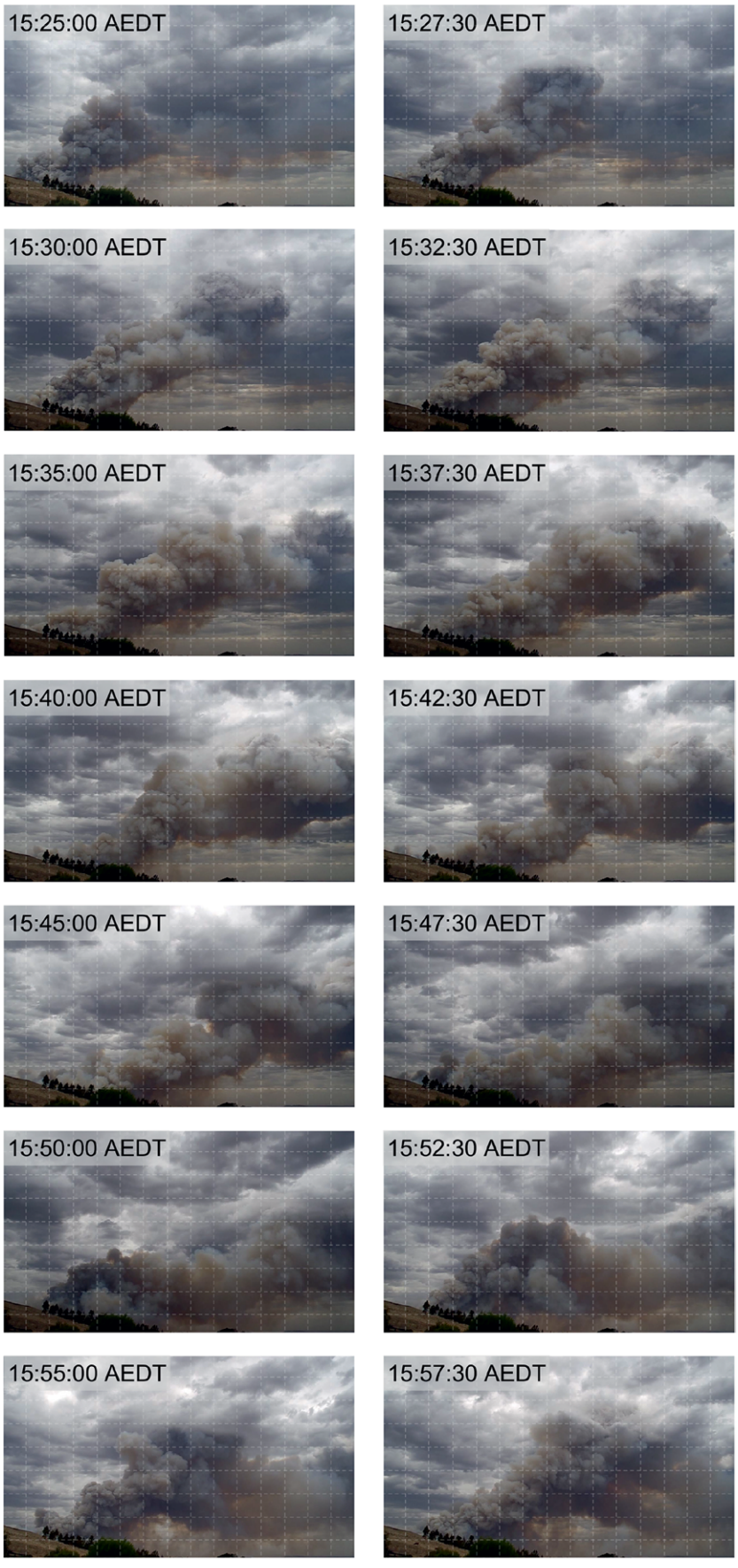

Fig. 5. Side-profile images of the Mount Bolton plume at intervals of 2 min, 30 s. Times are given in AEDT. Stills are taken from time lapse at a location 7.5 km southwest of the fire (37.426°S, 143.647°E). Time-lapse video covers the period 1430–1555 AEDT.

is noticeably more upright than from 1540 AEDT onward when it becomes more variable in the axis of its bend.

From 1430 to 2030 AEDT, the UQ-XPOL collected 2,845 RHI scans, at a rate of one scan approximately every 3–6 s at several azimuths 5 km from the fire. From 1520 AEDT, the radar conducted RHI scans along the azimuth 105°, which as shown in Fig. SB1g aligned approximately along the fire's primary axis of spread for the following hour. At the beginning of this period, the UQ-XPOL simultaneously observed the convective plume developing to a height of 6 km and a developing rain shower immediately downwind, though it is inconclusive whether this shower was initiated earlier by pyrocumulus from the fire. Figure 6 shows the reflectivity Z_H, differential reflectivity Z_{DR}, and correlation coefficient at zero lag (CC) from the UQ-XPOL at 1518 AEDT when the crown fire dominated the fire's behavior (see supplemental animation Fig. ES9).

The dashed reference line at 17 km in Figs. 6a–c separates the two notable reflectivity cores for investigating the polarimetric variables. At less than 17 km, the two beams were correlated poorly in the plume (CC less than 0.5), which is indicative of rough, nonspherical targets (Fig. 6c). This large turret of debris in the plume (Z_H over 30 dBZ)

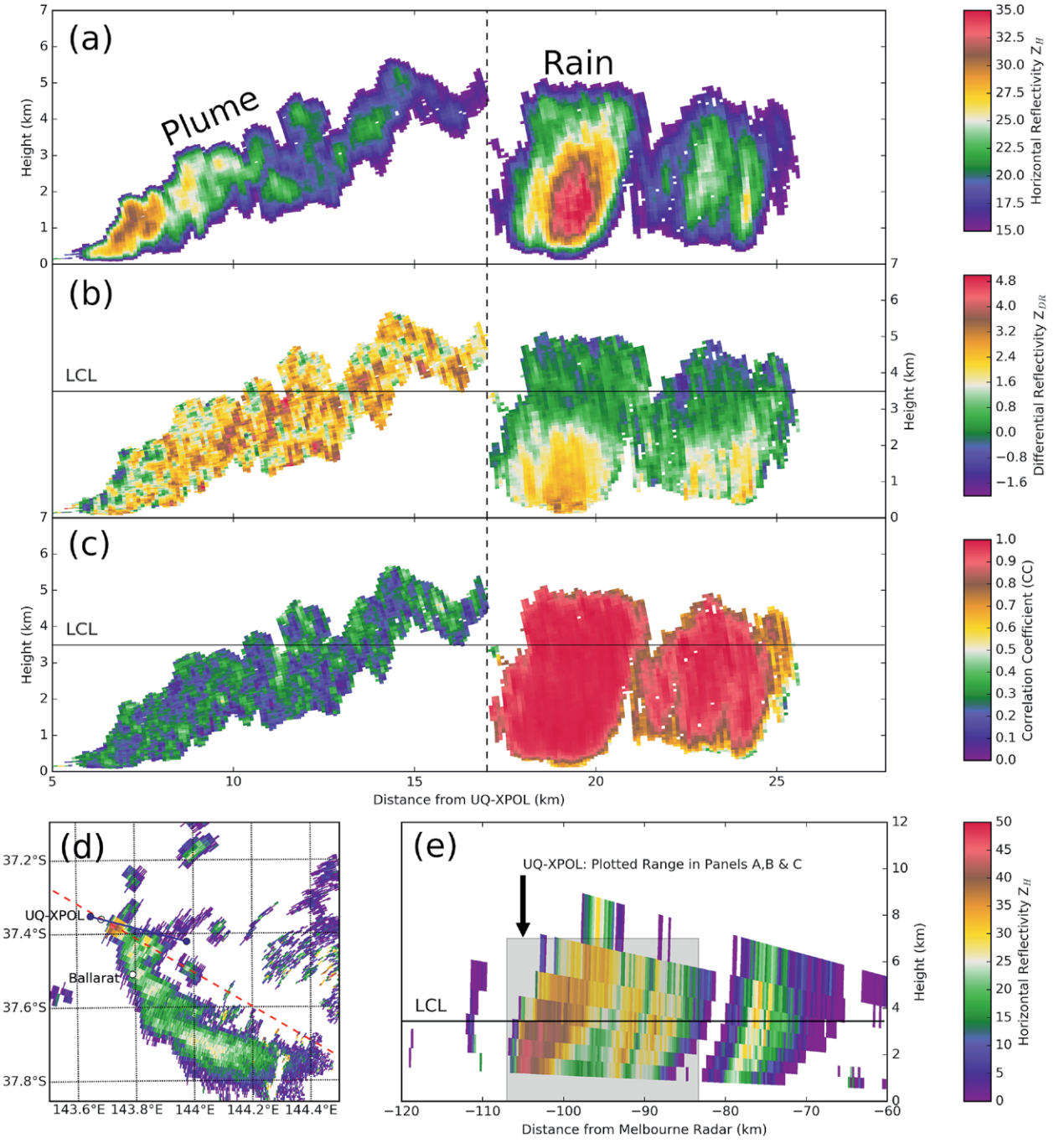

FIG. 6. Radar signatures of fire plume characteristics at 1518 AEDT from the UQ-XPOL deployed 5 km to the west of the fire and the Bureau of Meteorology's Melbourne radar 150 km to the southeast of the fire. Shown are the (a) reflectivity, (b) Z_{DR}, and (c) CC from the UQ-XPOL scanning at 105° (true north). Gates of weak returns (Z_H > 12 dBZ) and ground clutter (V_R = 0 ± 0.5 m s^{-1}) are removed. (d) The PPI reflectivity at 1.2° elevation. (e) A reconstructed RHI at 270° bearing from the Melbourne radar. The reconstructed RHI is indicated by the red dashed line in (d), while the blue line indicates the bearing and plotted range of the UQ-XPOL. The LCL is marked in the dual-polarization results in (b) and (c), as well as in the reconstructed RHI in (e). The gray-shaded rectangle in (e) is the approximate region presented in (a)–(c).

is a product of the large area of crown fire activity from 1430 AEDT (Figs. SB1a,d). This turret showed the strongest returns of Z_H within the plume, though reflectivity cores were also evident in the reflectivity of the Dereel fire through the entire period examined (see Fig. ES9). The Z_{DR} signature within the plume was strongly positively polarized, with a mean of 2.2 dBZ. The distribution was substantially more spread out in

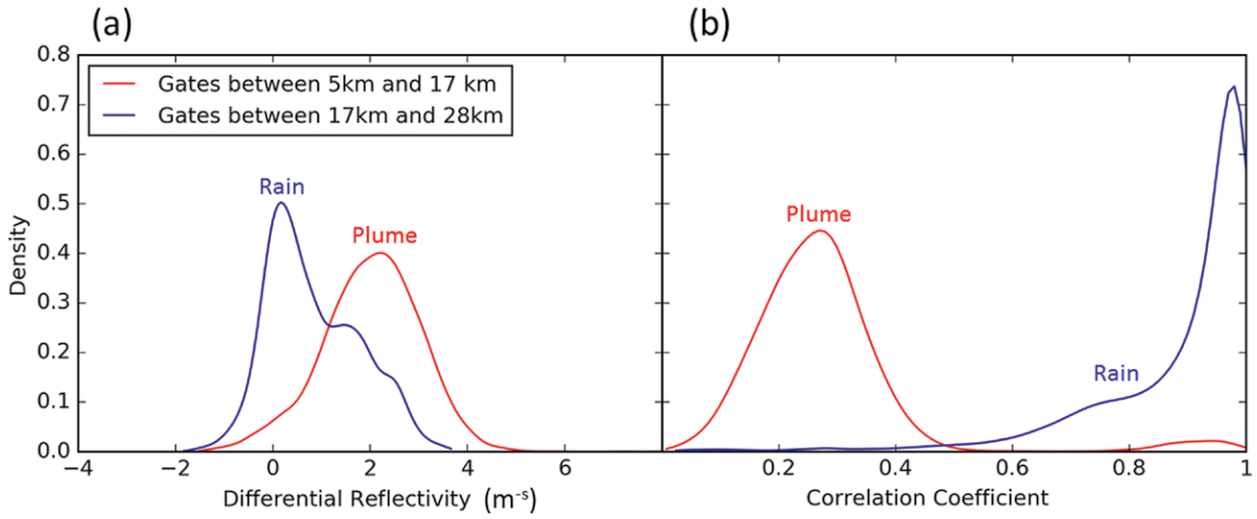

Fig. 7. Probability density functions for (a) Z_{DR} and (b) CC for all radar gates shown in Fig. 6 between 5 and 17 km (red) and between 17 and 28 km (blue) at 1518 AEDT.

the plume than in the second reflectivity core, consistent with the findings of Melnikov et al. (2009), with the probability density functions for CC confirming the differences between the two cores as per Fig. 7b.

The high values of CC (values near 1) in the core at approximately 20 km are consistent with that of rain, with the high correlation of the beams indicating near-spherical rain droplets (Figs. 6c and 7b). The signature of decreasing Z_{DR} with height below the lifting condensation level in the core at 20 km (Figs. 6b and 7a) is also consistent with coalescing droplets (Kumjian and Prat 2014). This is the only notable difference in the dual-polarization characteristics above and below the lifting condensation level (LCL).

A shortcoming of the RHI scan strategy at the Mount Bolton fire was that it remains unclear from the data whether this convective rain activity was a result of the fire. The Bureau of Meteorology S-band radar indicates the formation of multiple convective rainstorms around this time in nearby regions (Figs. 6d,e), as is common on fire weather days with unstable midlevels (Peterson et al. 2017b). Lightning observations[1] revealed that a thunderstorm did not mature until it was more than 50 km downwind, and therefore the Mount Bolton fire cannot not be considered a pyroCb event. Although it is possible that relatively weak lightning activity could have occurred in the plume that was not detected by the ground-based network [e.g., as noted for a case study in the United States with weak cloud-to-cloud lightning strokes (Lang et al. 2014)], these observations demonstrate that a large amount of lightning activity did not occur for the Mount Bolton case. This is in contrast to the strong lightning activity that was clearly observed for the pyroCbs on Black Saturday (Dowdy et al. 2017). While the areas of crown fire activity and the active fire front, as well as the rates of spread, for the Mount Bolton fire were not extreme compared to many pyroconvection examples, to date there have been no attempts to link radar signatures of any sort with the metric of fire severity (Fromm et al. 2006; Rosenfeld et al. 2007; Peterson et al. 2015).

Spectrum width observations from the Mount Bolton wildfire. Spectrum width σ_v is a metric that has, to date, received little attention as a variable for analyzing the turbulent flow within the convective plumes of wildfires since it was first noted anecdotally by Lhermitte (1969). Defined as the standard deviation of V_R, spectrum width provides a metric of dispersion in radial velocity within each gate volume, which is often attributable to turbulence (Istok and Doviak 1986). Figure 8 shows the distribution of σ_v, along with Z_H, for the Mount Bolton fire from 1515 to 1545 AEDT when the crown fire and spotting dominated the fire's behavior (Fig. 5).

The signature of spectrum width in Fig. 8 shows consistently lower values for the zone on the leeward side of the plume. The LCL is shown in Fig. 8 to illustrate an approximate depth of the pyrocumulus and how it relates to the buoyant and turbulent properties of the plume. Using the spectrum width

[1] Derived from the commercial provider Global Position and Tracking System Pty. Ltd. Australia (GPATS) based on the time of arrival of the electromagnetic disturbance propagating away from the lightning discharge as recorded at a network of ground-based radio receivers (Cummins and Murphy 2009).

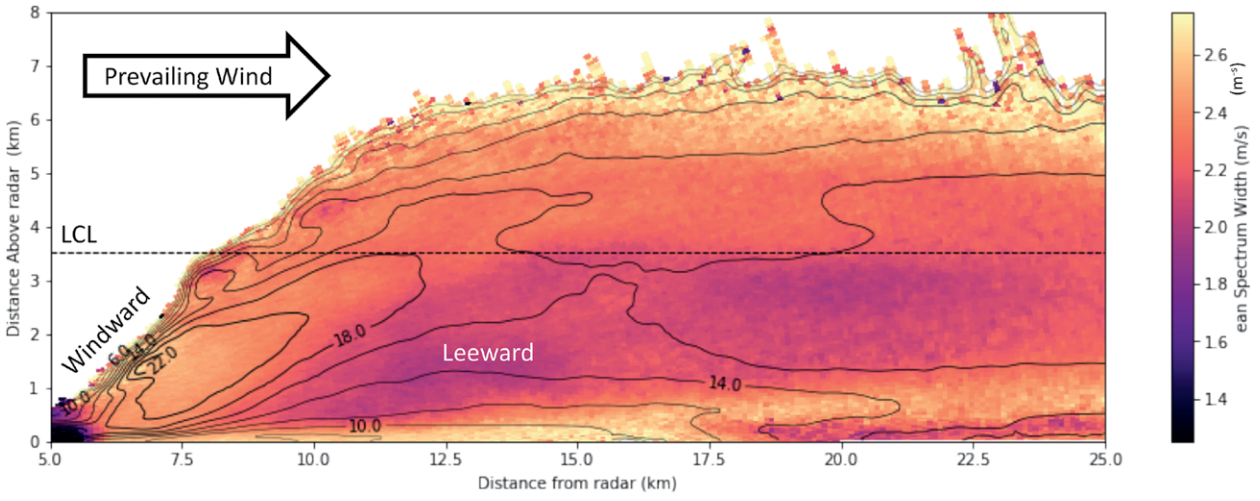

Fig. 8. Mean spectrum width, as well as reflectivity (contours every 2 dBZ from 10 dBZ), for the period 1515–1545 AEDT. The LCL calculated for the period being averaged is marked by the dashed line.

as an approximation of the distribution of turbulence, the structure of the turbulent plume becomes clear. The region of higher spectrum width indicates the position of the turbulent plume at its greatest intensity: over the 30-min period on the windward side of the plume in Fig. 8. This area is indicative of the increased shear, where conditions are likely to favor the development of horizontal axis vortices within the plume at its most upright. An important observation is the sharp boundary of Z_H (contours in Fig. 8) in this windward region compared to the leeside. The lower gradient of Z_H in this leeward zone is largely a product of the bending in the plume over time, including periods such as 1550 AEDT in Fig. 5. This offers a plausible explanation for the decreased σ_v and, thus, turbulence in the leeward zone marked in Fig. 8. The implication of this is that during periods when the plume is bent over with weaker updrafts, the turbulence is decreased with lower reflectivity (debris). This is in contrast to the periods with stronger updrafts and increased turbulence that are associated with the transportation of a higher density of debris.

The analysis of spectrum width demonstrates a practical way to validate the turbulent process of wildfire plumes with respect to fire behavior. Such results align with the model analysis of Thurston et al. (2017), who demonstrated a similar distribution of turbulence. Firebrands, carried within the turbulent plume and mapped by the spectrum width, ignited a number of spot fires up to 6 km from the fire ground (Fig. SB1h). Such spotting distances are still at the lower end of the scale compared to other Australian examples such as the Black Saturday event (Cruz et al. 2012). Spot fires at a distance of greater than a kilometer ahead of the fire represent a serious firefighting hazard (Koo et al. 2010), so the turbulent structures that govern their transport are worth further investigation via the presented method. These results highlight the wealth of data available on the plume dynamics in radar that can feed into pyroconvection and fire behavior case studies, in contrast to multiple studies where only air- or spaceborne analyses of the processes are used.

SUMMARY AND FUTURE WORK OF THE BCPE. We have outlined the initial findings from the BCPE field campaign from two wildfires and one prescribed burn in Australia; these results highlight the capability of mobile and dual-polarization Doppler radar for the study of pyroconvection. To date, there have been no published investigations of the use of mobile or dual-polarization radar for investigating the dynamics and fire–atmosphere interaction. These observations provide evidence of unique insights into pyroconvection that can be gained using mobile radar. Specific advances can be gained by taking advantage of reflectivity, dual-polarization, and spectrum-width analysis techniques that have their origins in storm and tornado research, but have seldom been used for wildfire applications.

The implications of the results presented highlight the significant need for further research into pyroconvection using radar. Given that quantitative data for extreme fire behavior from pyroconvection is rarely collected, and that such events have severe consequences, data collection by radar presents a temporally and spatially continuous data source that needs to be tied more explicitly to fire behavior. The resolution and range of the UQ-XPOL dataset show for the first time the ability of X-band radar to identify the

relatively finescale structures (on the order of hundreds of meters and 30-s resolution) shown in the Dereel fire and the vortices in the Apsey West prescribed burn. Future observations of this nature will be important for understanding some of the aspects of storm-scale convection from fires. The Mount Bolton results highlight the strong potential for the operational use of polarimetric characteristics to detect, isolate (e.g., as distinct from rain regions), and analyze wildfire plumes to improve our understanding of convective development in the otherwise complex convective environment of unstable extreme fire weather days. Given that the convective plumes of wildfires are a primary mechanism for producing long-range spot fires, the spectrum-width results indicate the potential role that X-band radar can play in the development and validation of predictive tools for spotting behavior.

Combined with the ground validation of fire behavior, radar data matching the characteristic length and time scales of vigorous convective plumes present an unexplored platform for investigating the structures of the plume. Future work of the BCPE will focus on the synthesis of the fire behavior and radar results; this has received little attention to date. A better understanding of these important turbulent structures can feed into enhanced situational awareness for fire managers and behavior analysts, where the transfer of knowledge will be a key output in the ongoing work of the BCPE. Through effective visualization of radar-observed plume processes from fire-ground case studies, a deeper understanding of the kinematics of pyroconvection can be gained. This could then serve to give heightened situational awareness and more scientific "lessons learned" to fire managers.

Given the losses of life and property caused by pyroconvective wildfires and the poorly understood nature of storm-scale convective structures above these events, the observations presented highlight the need for expansion in research when using this approach. The UQ-XPOL has shown that such mobile radar options have the sensitivity, resolution, and range to resolve the convective structures above large wildfires. An expanded use of this approach represents a logical extension of approaches developed in the thunderstorm and tornado research community. As well, it represents a significant tool to improve firefighting capabilities internationally. Field observations of pyroconvection by UQ-XPOL will be useful for collaborations with the international research community to help improve our understanding and modeling of high-impact wildfire.

ACKNOWLEDGMENTS. The BCPE was made possible by the contributions of Roland Barthelemy, Michael Gray, Christopher Chambers, and Joshua Soderholm in technical and field support. The Country Fire Authority, Queensland Fire and Emergency Services, and the University of Queensland (UQ) (through collaborative industry engagement funding) provided the financial support for the experiment. The Australian Bureau of Meteorology has provided significant and ongoing in-kind support for the project along with the Victorian Department of Environment, Land, Water and Property; the New South Wales Rural Fire Service; and the Queensland Parks and Wildlife Service. NM was partially supported by Advance Queensland, AG was funded by a UQ fellowship, and AD was supported by the Australian Government's National Environmental Science Programme. Special thanks to Tim Wells and Tim McKern for providing wildfire field campaign support and to José Torero, Claire Yeo, Andrew Sturgess, Laurence McCoy, and Kevin Parkyn, as well as the forecasters, FBANs, and volunteers, who enabled the safe success of the research. We thank Kevin Tory, Alain Protat, and Peter May from the Australian Bureau of Meteorology for their insightful comments on the manuscript. Additional photography and video provided by Wayne Rigg and John Holgate.

REFERENCES

Alexander, M. E, and D. A. Thomas, 2003: Wildland fire behavior case studies and analyses: value, approaches, and practical uses. *Fire Management Today*, Vol. 63, No. 3, 4–8, www.fs.fed.us/fire/fmt/fmt_pdfs/fmt63-3.pdf.

——, and M. G. Cruz, 2006: Evaluating a model for predicting active crown fire rate of spread using wildfire observations. *Can. J. For. Res.*, **36**, 3015–3028, https://doi.org/10.1139/x06-174.

Banta, R. M., L. D. Olivier, E. T. Holloway, R. A. Kropfli, B. W. Bartram, R. E. Cupp, and M. J. Post, 1992: Smoke-column observations from two forest fires using Doppler lidar and Doppler radar. *J. Appl. Meteor.*, **31**, 1328–1349, https://doi.org/10.1175/1520-0450(1992)031<1328:SCOFTF>2.0.CO;2.

Baum, T. C., L. Thompson, and K. Ghorbani, 2015: The nature of fire ash particles: Microwave material properties, dynamic behavior, and temperature correlation. *IEEE J. Sel. Top. Appl. Earth Obs. Remote Sens.*, **8**, 480–492, https://doi.org/10.1109/JSTARS.2014.2386394.

Biggerstaff, M. I., and Coauthors, 2005: The Shared Mobile Atmospheric Research and Teaching Radar: A collaboration to enhance research and teaching. *Bull. Amer. Meteor. Soc.*, **86**, 1263–1274, https://doi.org/10.1175/BAMS-86-9-1263.

Bluestein, H. B., 1999: A history of severe-storm-intercept field programs. *Wea. Forecasting*, **14**, 558–577,

https://doi.org/10.1175/15200434(1999)014<0558:AHOSSI>2.0.CO;2.

——, A. L. Pazmany, J. C. Galloway, and R. E. McIntosh, 1995: Studies of the substructure of severe convective storms using a mobile 3-mm-wavelength Doppler radar. *Bull. Amer. Meteor. Soc.*, **76**, 2155–2169, https://doi.org/10.1175/1520-0477(1995)076<2155:SOTSOS>2.0.CO;2.

——, and Coauthors, 2014: Radar in atmospheric sciences and related research: Current systems, emerging technology, and future needs. *Bull. Amer. Meteor. Soc.*, **95**, 1850–1861, https://doi.org/10.1175/BAMS-D-13-00079.1.

Bureau of Meteorology, 2016: Australia in summer 2015–16. Bureau of Meteorology, www.bom.gov.au/climate/current/season/aus/archive/201602.summary.shtml.

Byram, G. M., 1954: Atmospheric conditions related to blowup fires. Southeastern Forest Experiment Station Paper 35, U.S. Forest Service, Asheville, NC, 34 pp., www.srs.fs.usda.gov/pubs/sp/sp_se035.pdf.

——, 1959: Forest fire behavior. *Forest Fire: Control and Use*, K. P. Davis, Ed., McGraw Hill, 90–123.

——, and R. N. Nelson, 1951: The possible relation of air turbulence to erratic fire behavior in the Southeast. *Fire Control Notes*, **12**, 1–8.

Chandrasekar, V., R. Keränen, S. Lim, and D. Moisseev, 2013: Recent advances in classification of observations from dual polarization weather radars. *Atmos. Res.*, **119**, 97–111, https://doi.org/10.1016/j.atmosres.2011.08.014.

Clark, T. L., L. Radke, J. Coen, and D. Middleton, 1999: Analysis of small-scale convective dynamics in a crown fire using infrared video camera imagery. *J. Appl. Meteor.*, **38**, 1401–1420, https://doi.org/10.1175/1520-0450(1999)038<1401:AOSSCD>2.0.CO;2.

Clements, C. B., and A. J. Oliphant, 2014: The California State University Mobile Atmospheric Profiling System: A facility for research and education in boundary layer meteorology. *Bull. Amer. Meteor. Soc.*, **95**, 1713–1724, https://doi.org/10.1175/BAMS-D-13-00179.1.

——, and Coauthors, 2007: Observing the dynamics of wildland grass fires: FireFlux—A field validation experiment. *Bull. Amer. Meteor. Soc.*, **88**, 1369–1382, https://doi.org/10.1175/BAMS-88-9-1369.

Cruz, M. G., A. L. Sullivan, J. S. Gould, N. C. Sims, A. J. Bannister, J. J. Hollis, and R. J. Hurley, 2012: Anatomy of a catastrophic wildfire: The Black Saturday Kilmore East fire in Victoria, Australia. *For. Ecol. Manage.*, **284**, 269–285, https://doi.org/10.1016/j.foreco.2012.02.035.

——, ——, and M. E. Alexander, 2014: Fire behaviour knowledge in Australia: Knowledge gaps and fire behaviour analyst (FBAN) training revision plan. Client Rep. EP145697, CSIRO Ecosystems Sciences, Canberra, ACT, Australia, 22 pp.

Cummins, K. L., and M. J. Murphy, 2009: An overview of lightning locating systems: History, techniques, and data uses, with an in-depth look at the U.S. NLDN. *IEEE Trans. Electromagn. Compat.*, **51**, 499–518, https://doi.org/10.1109/TEMC.2009.2023450.

Cunningham, P., and M. J. Reeder, 2009: Severe convective storms initiated by intense wildfires: Numerical simulations of pyro-convection and pyro-tornadogenesis. *Geophys. Res. Lett.*, **36**, L12812, https://doi.org/10.1029/2009GL039262.

——, S. L. Goodrick, M. Y. Hussaini, and R. R. Linn, 2005: Coherent vortical structures in numerical simulations of buoyant plumes from wildland fires. *Int. J. Wildland Fire*, **14**, 61–75, https://doi.org/10.1071/WF04044.

Dowdy, A. J., 2018: Climatological variability of fire weather in Australia. *J. Appl. Meteor. Climatol.*, **57**, 221–234, https://doi.org/10.1175/JAMC-D-17-0167.1.

——, G. A. Mills, K. Finkele, and W. de Groot, 2009: Australian fire weather as represented by the McArthur forest fire danger index and the Canadian forest fire weather index. Centre for Australian Weather and Climate Research Tech. Rep. 10, 84 pp., www.cawcr.gov.au/technical-reports/CTR_010.pdf.

——, M. D. Fromm, and N. McCarthy, 2017: Pyrocumulonimbus lightning and fire ignition on Black Saturday in southeast Australia. *J. Geophys. Res. Atmos.*, **122**, 7342–7354, https://doi.org/10.1002/2017JD026577.

Ferguson, E., 2016: Reframing rural fire management: Report of the special inquiry into the January 2016 Waroona fire. Public Sector Commission, Government of Western Australia, Perth, WA, 263 pp., https://publicsector.wa.gov.au/document/reframing-rural-fire-management-report-special-inquiry-january-2016-waroona-fire.

Forthofer, J. M., and S. L. Goodrick, 2011: Review of vortices in wildland fire. *J. Combust.*, **2011**, 984363, https://doi.org/10.1155/2011/984363.

——, R. Linn, J. Sauer, and B. Butler, 2009: Investigating causes of large scale fire whirls using numerical simulation. *Eighth Symp. on Fire and Forest Meteorology*, Kalispell, MT, Amer. Meteor. Soc., 4.2, https://ams.confex.com/ams/pdfpapers/156344.pdf.

Fric, T. F., and A. Roshko, 1994: Vortical structure in the wake of a transverse jet. *J. Fluid Mech.*, **279**, 1–47, https://doi.org/10.1017/S0022112094003800.

Fromm, M., R. Bevilacqua, R. Servranckx, J. Rosen, J. P. Thayer, J. Herman, and D. Larko, 2005: Pyro-cumulonimbus injection of smoke to the stratosphere:

Observations and impact of a super blowup in northwestern Canada on 3–4 August 1998. *J. Geophys. Res.*, **110**, D08205, https://doi.org/10.1029/2004JD005350.

——, A. Tupper, D. Rosenfeld, R. Servranckx, and R. McRae, 2006: Violent pyro-convective storm devastates Australia's capital and pollutes the stratosphere. *Geophys. Res. Lett.*, **33**, L05815, https://doi.org/10.1029/2005GL025161.

——, D. T. Lindsey, R. Servranckx, G. Yue, T. Trickl, R. Sica, P. Doucet, and S. Godin-Beekmann, 2010: The untold story of pyrocumulonimbus. *Bull. Amer. Meteor. Soc.*, **91**, 1193–1209, https://doi.org/10.1175/2010BAMS3004.1.

Graham, H. E., 1951: A firewhirl of tornadic violence. *Fire Control Notes*, **13**, 22–24.

Haynes, K., J. Handmer, J. McAneney, A. Tibbits, and L. Coates, 2010: Australian bushfire fatalities 1900–2008: Exploring trends in relation to the 'Prepare, stay and defend or leave early' policy. *Environ. Sci. Policy*, **13**, 185–194, https://doi.org/10.1016/j.envsci.2010.03.002.

Heilman, W. E., C. B. Clements, S. Seto, X. Bian, N. S. Skowronski, and J. L. Hom, 2015: Observations of fire-induced turbulence regimes during low-intensity wildland fires in forested environments: Implications for smoke dispersion. *Atmos. Sci. Lett.*, **16**, 453–460, https://doi.org/10.1002/asl.581.

Helmus, J. J., and S. M. Collis, 2016: The Python ARM Radar Toolkit (Py-ART), a library for working with weather radar data in the Python programming language. *J. Open Res. Software*, **4**, 25, https://doi.org/10.5334/jors.119.

Hirsch, K., and D. Martell, 1996: A review of initial attack fire crew productivity and effectiveness. *Int. J. Wildland Fire*, **6**, 199–215, https://doi.org/10.1071/WF9960199.

Istok, M. J., and R. J. Doviak, 1986: Analysis of the relation between Doppler spectral width and thunderstorm turbulence. *J. Atmos. Sci.*, **43**, 2199–2214, https://doi.org/10.1175/1520-0469(1986)043<2199:AOTRBD>2.0.CO;2.

Jones, D. A., W. Wang, and R. Fawcett, 2009: High-quality spatial climate data-sets for Australia. *Aust. Meteor. Oceanogr. J.*, **58**, 233, https://doi.org/10.22499/2.5804.003.

Jones, T. A., and S. A. Christopher, 2010a: Satellite and radar observations of the 9 April 2009 Texas and Oklahoma grassfires. *Bull. Amer. Meteor. Soc.*, **91**, 455–460, https://doi.org/10.1175/2009BAMS2919.1.

——, and ——, 2010b: Satellite and radar remote sensing of southern plains grass fires: A case study. *J. Appl. Meteor. Climatol.*, **49**, 2133–2146, https://doi.org/10.1175/2010JAMC2472.1.

Koo, E., P. J. Pagni, D. R. Weise, and J. P. Woycheese, 2010: Firebrands and spotting ignition in large-scale fires. *Int. J. Wildland Fire*, **19**, 818–843, https://doi.org/10.1071/WF07119.

Kumjian, M. R., and O. P. Prat, 2014: The impact of raindrop collisional processes on the polarimetric radar variables. *J. Atmos. Sci.*, **71**, 3052–3067, https://doi.org/10.1175/JAS-D-13-0357.1.

Lang, T. J., S. A. Rutledge, B. Dolan, P. Krehbiel, W. Rison, and D. T. Lindsey, 2014: Lightning in wildfire smoke plumes observed in Colorado during summer 2012. *Mon. Wea. Rev.*, **142**, 489–507, https://doi.org/10.1175/MWR-D-13-00184.1.

Lareau, N. P., and C. B. Clements, 2016: Environmental controls on pyrocumulus and pyrocumulonimbus initiation and development. *Atmos. Chem. Phys.*, **16**, 4005–4022, https://doi.org/10.5194/acp-16-4005-2016.

——, and ——, 2017: The mean and turbulent properties of a wildfire convective plume. *J. Appl. Meteor. Climatol.*, **56**, 2289–2299, https://doi.org/10.1175/JAMC-D-16-0384.1.

Lhermitte, R. M., 1969: Note on the observation of small-scale atmospheric turbulence by Doppler radar techniques. *Radio Sci.*, **4**, 1241–1246, https://doi.org/10.1029/RS004i012p01241.

Marquis, J., Y. Richardson, J. Wurman, and P. Markowski, 2008: Single-and dual-Doppler analysis of a tornadic vortex and surrounding storm-scale flow in the Crowell, Texas, supercell of 30 April 2000. *Mon. Wea. Rev.*, **136**, 5017–5043, https://doi.org/10.1175/2008MWR2442.1.

McAneney, J., K. Chen, and A. Pitman, 2009: 100-years of Australian bushfire property losses: Is the risk significant and is it increasing? *J. Environ. Manage.*, **90**, 2819–2822, https://doi.org/10.1016/j.jenvman.2009.03.013.

McArthur, A. G., 1967: Fire behaviour in eucalypt forests. Forestry and Timber Bureau Leaflet 107, 36 pp.

McRae, D. J., and M. D. Flannigan, 1990: Development of large vortices on prescribed fires. *Can. J. For. Res.*, **20**, 1878–1887, https://doi.org/10.1139/x90-252.

——, B. J. Stocks, and C. J. Ogilvie, 1989: Fire acceleration on large-scale convection burns. *Proc. 10th Conf. on Fire and Forest Meteorology*, Ottawa, ON, Canada, Forestry Canada, 101–107.

McRae, R. H. D., J. J. Sharples, S. R. Wilkes, and A. Walker, 2013: An Australian pyro-tornadogenesis event. *Nat. Hazards*, **65**, 1801–1811, https://doi.org/10.1007/s11069-012-0443-7.

——, ——, and M. Fromm, 2015: Linking local wildfire dynamics to pyroCb development. *Nat. Hazards Earth Syst. Sci.*, **15**, 417–428, https://doi.org/10.5194/nhess-15-417-2015.

Melnikov, V. M., D. S. Zrnić, R. M. Rabin, and P. Zhang, 2008: Radar polarimetric signatures of fire plumes in Oklahoma. *Geophys. Res. Lett.*, **35**, L14815, https://doi.org/10.1029/2008GL034311.

——, ——, and ——, 2009: Polarimetric radar properties of smoke plumes: A model. *J. Geophys. Res.*, **114**, D21204, https://doi.org/10.1029/2009JD012647.

Morton, B. R., 1957: Buoyant plumes in a moist atmosphere. *J. Fluid Mech.*, **2**, 127–144, https://doi.org/10.1017/S0022112057000038.

——, and A. Ibbetson, 1996: Jets deflected in a crossflow. *Exp. Therm. Fluid Sci.*, **12**, 112–133, https://doi.org/10.1016/0894-1777(95)00097-6.

Peace, M., T. Mattner, G. Mills, J. Kepert, and L. McCaw, 2015: Fire-modified meteorology in a coupled fire–atmosphere model. *J. Appl. Meteor. Climatol.*, **54**, 704–720, https://doi.org/10.1175/JAMC-D-14-0063.1.

Peterson, D. A., E. J. Hyer, J. R. Campbell, M. D. Fromm, J. W. Hair, C. F. Butler, and M. A. Fenn, 2015: The 2013 Rim fire: Implications for predicting extreme fire spread, pyroconvection, and smoke emissions. *Bull. Amer. Meteor. Soc.*, **96**, 229–247, https://doi.org/10.1175/BAMS-D-14-00060.1.

——, M. D. Fromm, J. E. Solbrig, E. J. Hyer, M. L. Surratt, and J. R. Campbell, 2017a: Detection and inventory of intense pyroconvection in western North America using *GOES-15* daytime infrared data. *J. Appl. Meteor. Climatol.*, **56**, 471–493, https://doi.org/10.1175/JAMC-D-16-0226.1.

——, E. J. Hyer, J. R. Campbell, J. E. Solbrig, and M. D. Fromm, 2017b: A conceptual model for development of intense pyrocumulonimbus in western North America. *Mon. Wea. Rev.*, **145**, 2235–2255, https://doi.org/10.1175/MWR-D-16-0232.1.

Plucinski, M. P., G. J. McCarthy, J. J. Hollis, and J. S. Gould, 2012: The effect of aerial suppression on the containment time of Australian wildfires estimated by fire management personnel. *Int. J. Wildland Fire*, **21**, 219–229, https://doi.org/10.1071/WF11063.

Potter, B. E., 2012a: Atmospheric interactions with wildland fire behaviour—I. Basic surface interactions, vertical profiles and synoptic structures. *Int. J. Wildland Fire*, **21**, 779–801, https://doi.org/10.1071/WF11128.

——, 2012b: Atmospheric interactions with wildland fire behaviour—II. Plume and vortex dynamics. *Int. J. Wildland Fire*, **21**, 802–817, https://doi.org/10.1071/WF11129.

Radke, L. F., and Coauthors, 1991: Particulate and trace gas emissions from large biomass fires in North America. *Global Biomass Burning: Atmospheric, Climatic, and Biospheric Implications*, J. S. Levine, Ed., MIT Press, 209–224.

Reid, D. G., and R. G. Vines, 1972: A radar study of the smoke plume from a forest fire. Division of Applied Chemistry Tech. Paper, Commonwealth Scientific and Industrial Research Organisation, Melbourne, VIC, Australia, 12 pp.

Reid, J. S., R. Koppmann, T. F. Eck, and D. P. Eleuterio, 2005: A review of biomass burning emissions. Part II: Intensive physical properties of biomass burning particles. *Atmos. Chem. Phys.*, **5**, 799–825, https://doi.org/10.5194/acp-5-799-2005.

Robin, A. G., 1957: Weather conditions associated with the broadford fire. *Aust. Meteor. Oceanogr. J.*, **18**, 30–43.

Rosenfeld, D., M. Fromm, J. Trentmann, G. Luderer, M. O. Andreae, and R. Servranckx, 2007: The Chisholm firestorm: Observed microstructure, precipitation and lightning activity of a pyro-cumulonimbus. *Atmos. Chem. Phys.*, **7**, 645–659, https://doi.org/10.5194/acp-7-645-2007.

Seto, D., C. B. Clements, and W. E. Heilman, 2013: Turbulence spectra measured during fire front passage. *Agric. For. Meteor.*, **169**, 195–210, https://doi.org/10.1016/j.agrformet.2012.09.015.

——, T. Strand, C. B. Clements, H. Thistle, and R. Mickler, 2014: Wind and plume thermodynamic structures during low-intensity subcanopy fires. *Agric. For. Meteor.*, **198–199**, 53–61, https://doi.org/10.1016/j.agrformet.2014.07.006.

Soderholm, J., H. McGowan, H. Richter, K. Walsh, T. Weckwerth, and M. Coleman, 2016: The Coastal Convective Interactions Experiment (CCIE): Understanding the role of sea breezes for hailstorm hotspots in eastern Australia. *Bull. Amer. Meteor. Soc.*, **97**, 1687–1698, https://doi.org/10.1175/BAMS-D-14-00212.1.

Thurston, W., J. D. Kepert, K. J. Tory, and R. J. B. Fawcett, 2017: The contribution of turbulent plume dynamics to long-range spotting. *Int. J. Wildland Fire*, **26**, 317–330, https://doi.org/10.1071/WF16142.

U.S. Forest Service, 2015: The rising cost of fire operations: Effects on the Forest Service's non fire work. U.S. Department of Agriculture, 16 pp., www.fs.fed.us/sites/default/files/2015-Fire-Budget-Report.pdf.

Wurman, J., J. Straka, E. Rasmussen, M. Randall, and A. Zahrai, 1997: Design and deployment of a portable, pencil-beam, pulsed, 3-cm Doppler radar. *J. Atmos. Oceanic Technol.*, **14**, 1502–1512, https://doi.org/10.1175/1520-0426(1997)014<1502:DADOAP>2.0.CO;2.

——, and Coauthors, 2012: The Second Verification of the Origins of Rotation in Tornadoes Experiment: VORTEX2. *Bull. Amer. Meteor. Soc.*, **93**, 1147–1170, https://doi.org/10.1175/BAMS-D-11-00010.1.